ADVANCED ENERGY MATERIALS
www.advenergymat.de

Interrelation Between External Pressure, SEI Structure, and Electrodeposit Morphology in an Anode-Free Lithium Metal Battery

Wei Liu, Yiteng Luo, Yuhang Hu, Zidong Chen, Qiang Wang, Yungui Chen, Naseem Iqbal, and David Mitlin**

The interrelation is explored between external pressure (0.1, 1, and 10 MPa), solid electrolyte interphase (SEI) structure/morphology, and lithium metal plating/stripping behavior. To simulate anode-free lithium metal batteries (AF-LMBs) analysis is performed on "empty" Cu current collectors in standard carbonate electrolyte. Lower pressure promotes organic-rich SEI and macroscopically heterogeneous, filament-like Li electrodeposits interspersed with pores. Higher pressure promotes inorganic F-rich SEI with more uniform and denser Li film. A "seeding layer" of lithiated pristine graphene (pG@Cu) favors an anion-derived F-rich SEI and promotes uniform metal electrodeposition, enabling extended electrochemical stability at a lower pressure. State-of-the-art electrochemical performance is achieved at 1MPa: pG-enabled half-cell is stable after 300 h (50 cycles) at 1 mA cm^{-2} rate —3 mAh cm^{-2} capacity (17.5 µm plated/stripped), with cycling Coulombic efficiency (CE) of 99.8%. AF-LMB cells with high mass loading NMC622 cathode (21 mg cm^{-2}) undergo 200 cycles with a CE of 99.4% at C/5-charge and C/2-discharge (1C = 178 mAh g^{-1}). Density functional theory (DFT) highlights the differences in the adsorption energy of solvated-Li^+ onto various crystal planes of Cu (100), (110), and (111), versus lithiated/delithiated (0001) graphene, giving insight regarding the role of support surface energetics in promoting SEI heterogeneity.

1. Introduction

Lithium metal is considered the ultimate choice for the next-generation anode in Li-based secondary batteries due to its high capacity (3860 $mAhg^{-1}$) and the associated low charging voltage.[1] However it is well-recognized that lithium electrodeposition/dissolution tends to be non-planar, with metal dendrites, metal voids, and an unstable solid electrolyte interphase (SEI). This in turn results in irreversible loss of active Li and poor Coulombic efficiency (CE), and in some cases internal short-circuiting. Lithium dendrites are deemed as the key culprit for the unacceptably shortened cycle and decreased safety of lithium metal batteries (LMBs) versus the established LIBs.[2] Significant efforts have been devoted to suppressing dendritic Li growth by adopting 3D current collectors,[3] artificial SEI membranes,[4] lithiophilic substrates,[5] and novel electrolyte systems including additives,[6] high-concentration electrolytes[7] and localized high-concentration electrolytes.[8] Approaches based on a "Li-seeding" layer on top of Cu foil have been explored, with Au,[9] Pt,[10] Ag,[11] and Sn[12] all being effective. Achieving planar and dense electrodeposition/dissolution is at the heart of LMBs development efforts.

Alkaline metal anode research has been historically based on thick Li-foils for cell evaluation, usually greater than 200 µm and

W. Liu, Y. Luo, Y. Hu, Z. Chen, Y. Chen
Institute of New-Energy and Low-Carbon Technology (INELT)
Sichuan University
Chengdu, Sichuan 610065, China
E-mail: weiliu@scu.edu.cn
W. Liu, Y. Chen
Engineering Research Center of Alternative Energy Materials & Devices
Ministry of Education
Sichuan University
Chengdu, Sichuan 610065, China

Q. Wang
School of Materials and Energy
Southwest University
Chongqing 400715, China
N. Iqbal
US-Pakistan Center for Advanced Studies (USPCAS-E)
National University of Sciences and Technology (NUST)
H-12, Islamabad 44000, Pakistan
D. Mitlin
Materials Science and Engineering Program & Texas Materials Institute
The University of Texas at Austin
Austin, TX 78712, USA
E-mail: david.mitlin@austin.utexas.edu

The ORCID identification number(s) for the author(s) of this article can be found under https://doi.org/10.1002/aenm.202302261

DOI: 10.1002/aenm.202302261

often in the 0.5 mm range. In such cases, the fraction of the metal anode that is electrodeposited/dissolved is only several percent, as 1 mAh cm^{-2} equals 5 microns of Li. This is a far cry from the often-quoted infinite volumetric expansion/contraction at every cycle. However, it is now recognized that to render Li metal truly advantageous over graphite both in terms of energy and cost, much thinner foils are necessary (< 50 µm, ideally < 25 µm).[13] Taking this consideration a step further, Anode-Free Lithium Metal Batteries (AF-LMBs), employ an "empty" Cu thin foil current collector with all the available Li being stored in the cathode. AF-LMBs demonstrate the capability to boost the cell gravimetric energy by ≈35% and volumetric energy by 80% as compared to graphite-anode-based LIBs.[14] AF-LMBs represent the most challenging of all LMB architectures due to the limited Li supply, as well as due to the difficulty of achieving planar electrodeposits on a Cu foil (100% DOD) versus on a pre-existing Li metal reservoir.[15]

Carbonate-based electrolytes employed by industry (e.g., 1 M $LiPF_6$ in EC:DEC:EMC with 5% FEC) would be the ideal choice for next-generation batteries due to their cost, ionic-conductivity, viscosity/wettability, and compatibility with high-voltage cathodes.[16] However, metal dendrites and overall poor CE makes carbonate-based solvents especially difficult with AF-LMBs. Instead, a range of novel electrolytes was found to extend the cycling stability of AF-LMBs, including ether electrolytes, fluorinated electrolytes, and ionic liquids.[17] Applying a nucleating layer on the current collector has also been explored.[3b] High static pressure (up to 10's of MPa) has been demonstrated to promote electrodeposition/dissolution stability and improved CE with AF-LMBs.[18] In practical cell stacks, including pouch cells and cylindrical batteries, the workable pressure is on the order of 1 MPa.[19] Researchers have demonstrated improved Li-metal reversibility by incorporating external pressure during cell operation, with several plausible explanations for the effect being brought forth.[18a,b,20] While external pressure is known to generally improve electrochemical performance, one limiting aspect of that approach are the cell separators. While "dry" polyolefin separators (PE/PP) may possess strength up to tens of MPa, they become substantially weaker when soaked in liquid electrolytes.[21] Consequently the wet separators become susceptible to tearing at high pressures. This further limits the external pressure that may be used in real battery stacks. Due to the propensity for dendrites and an unstable SEI in anode-free configurations, achieving extended cycling in AF-LMBs at practical pressures remains a highly challenging task.

The interrelations Li plating kinetics and the SEI structure or the support lithiophilicity have been treated in literature.[15a,22] What has not been explored is the more complex relationship between the externally applied stress, the current collector support structure/chemistry, the SEI, and the electrodeposition/dissolution process. In this study we employ a layer of pristine graphene directly coated onto the current collector (pG@Cu) to demonstrate how enhanced metal wetting can be a direct substitute for higher pressure in stabilizing the Li electrodeposition/dissolution behavior. It is shown that graphene-promoted lithium wetting enables stable electrodeposition/dissolution in an anode-free lithium metal battery (AF-LMB) at 1 MPa. The synergy between the pG seeding layer and low pressure of 1 MPa achieves planar Li deposition throughout prolonged cycling, delivering a Coulombic efficiency (CE) of 99.8% in half-cells and stable cycling of high-mass-loading full cells. A series of analytical and atomic simulation-based studies are undertaken to explain the mechanistic origin of this behavior.

2. Results and Discussion

Figure 1a demonstrates a custom-made battery PEEK cell that allows for measurement and control of the static pressure during electrochemical testing. The apparatus allows for cell operation in a liquid electrolyte under differing static pressure levels. The two-electrode cell is placed between two stainless-steel pillar electrodes that are connected to the battery tester. The upper side is connected to tightening bolts while the bottom side is directly placed upon the pressure sensor. The externally applied static pressure is then varied by screwing/unscrewing the bolts. A PTFE insulating ring is adopted to regulate the electrodeposit area. Before performing the electrodeposition experiments the baseline uncoated copper foil current collectors underwent the following conditioning treatment: A low current (50 µA cm^{-2}) lithiation step with a cut-off voltage of 0.01 V versus Li/Li^+ was adopted to remove the Cu surface oxides and to stabilize the solid electrolyte interphase (SEI). Two types of experiments were then performed: The experiments termed "lithiation" are meant to probe the structure of the SEI without incurring any metal plating, the lower cutoff voltage being 0.01 V. The experiments termed "plating", are meant to probe the structure of the lithium metal and of the associated SEI, where the lower voltage is determined by the plating overpotential and the upper voltage is set to 1 V versus Li/Li^+. For example, galvanostatic plating of Li at 1 mA cm^{-2} was carried out lasting for 3 h, corresponding to an area capacity of 3 mAh cm^{-2}. These galvanostatic profiles under varying static pressure are shown in Figure 1b. With pressure increasing from 0.1 to 1, and to 10 MPa the nucleation overpotential was lowered from 340 to 290, and to 150 mV, respectively.

The continuous and relatively flat overpotential present after the sharp nucleation peak is associated with metal grain growth,[5,23] although one could reasonably expect nucleation of additional grains to occur in parallel. The 0.1 MPa cells showed an incrementally larger growth-related overpotential, going from 100 to 150 mV as electrodeposition proceeded. The growth-related overpotential for the 1 and 10 MPa specimens was nearly identical at 45 mV. This trend qualitatively agrees with recent solid-state battery studies where the authors varied the externally applied pressure and directly monitored Li metal nucleation on a blank current collector foil.[24] The key finding was that with higher pressure, the number and the areal coverage of electrodeposited Li islands increased.[25] These chemo-mechanical effects are synonymous with a reduced kinetic barrier for grain nucleation and grain growth with increasing pressure. While the electrolyte media in this study is an organic liquid rather than LLZO solid, the nucleation-growth-pressure interrelations should be analogous. In both cases Li metal is nucleating and growing on a Cu foil. However, the two scenarios do have differences: with liquid electrolytes there is ongoing SEI formation and evolution, while the Li metal -LLZO interface is minimally reactive. The role of pressure in determining the SEI morphology and structure will be detailed later.

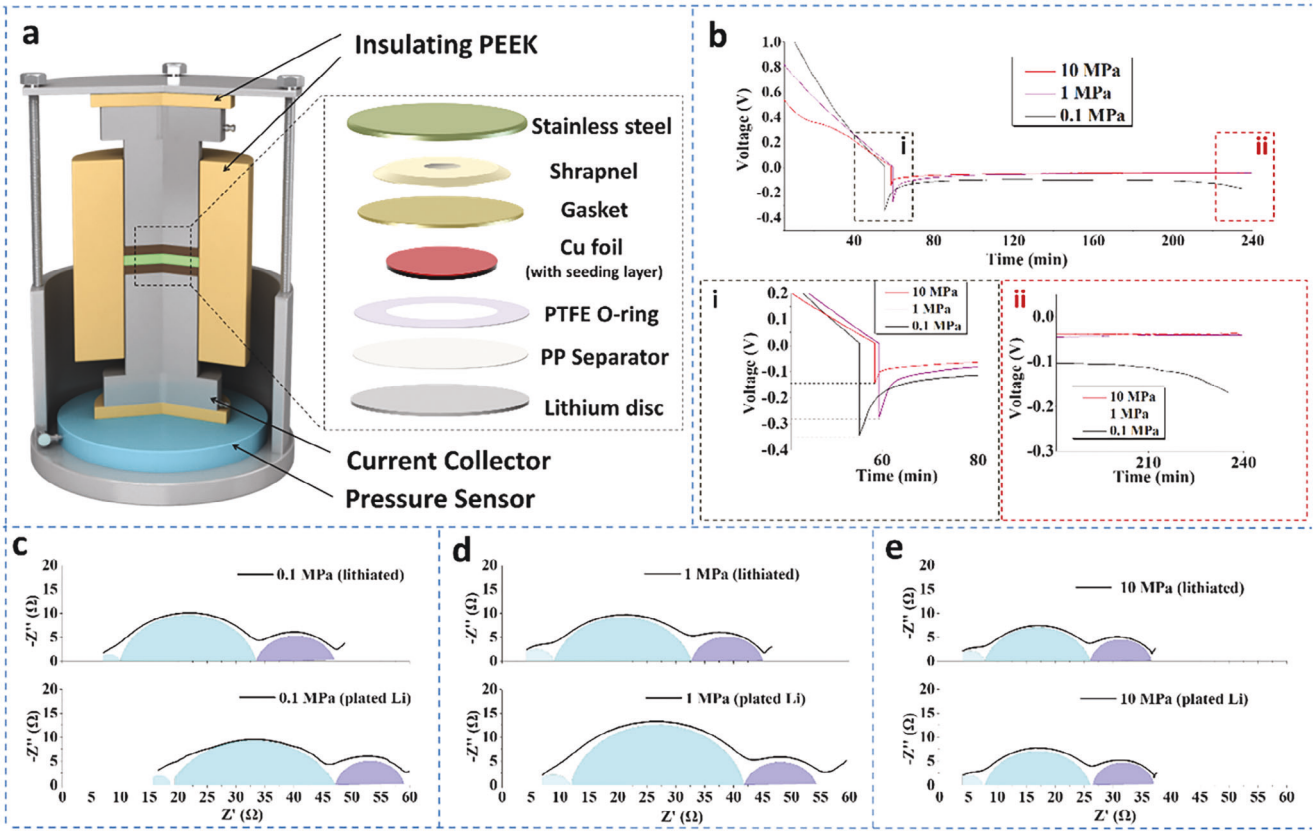

Figure 1. a) Diagram of the custom PEEK cell that allows pressure control during cell operation. b) Voltage profiles of Li plated onto Cu|Li at 1 mA cm^{-1}, with external pressure of 10, 1, or 0.1 MPa. Subpanels (i) and (ii) show expanded portions of the nucleation and growth sections, respectively. c–e) EIS spectra of Li|Cu that were lithiated to 0.01 V versus Li/Li$^+$ at 50 µA cm^{-2}, followed by plating of 3 mAh cm^{-2} at 1 mA cm^{-2}.

Electrochemical impedance spectroscopy (EIS) results of Li||Cu half-cells cells are compared in Figure 1c–e, with their corresponding equivalent circuits shown in Figure S1 (Supporting Information). Going from highest to lowest frequency, the three semicircles in the Nyquist plots represent the resistance of a dual-layered SEI (R_{SEI-1} and R_{SEI-2}) and the charge transfer resistance (R_{ct}).[26] A dual-layered SEI has been reported previously and is ascribed to a two-step surface film formation process, one being formed by immersion-based chemical reaction of Cu surface (CuO_x) with the $LiPF_6$-based electrolyte and the other being more relevant to further electrochemical electrolyte reduction.[27] In the state of being lithiated to 0.01 V, the cell's Ohmic resistance (R_{Ohm}) decreases with increasing pressure. The R_{Ohm} values are 6.1 Ω at 0.1 MPa, 2.8 Ω at 1 MPa, and 2.7 Ω at 10 MPa. This is ascribed to the improved electrical contact inside the cell, as pressure is not expected to affect ionic resistance in the electrolyte. Once the Li is plated, R_{Ohm} resistance of the cell actually increases. This is ascribed to degraded electrical contact due to poor coverage of the collector by the metal. The role of increasing pressure becomes quite significant in the plated state: R_{Ohm} values are 14.8 Ω at 0.1 MPa, 5.8 Ω at 1 MPa, and 2.7 Ω at 10 MPa. It will be demonstrated in the modeling results of the manuscript that external pressure is not just a physical flattening of metal islands to enable better contact with the collector. External pressure affects the metal nucleation and growth energetics, to some extent compensating for the unfavorable interfacial energetics between the Li electrodeposit and an unmodified Cu foil. As may be observed from **Table 1**, an external pressure of 10 MPa also serves to lower the SEI resistance and the charge transfer resistance, both in the lithiated and the plated states. If the metal electrodeposit is made more conformal through the application of external pressure, the SEI that forms on its surface would likewise be smoother and more geometrically uniform. This should be enough to lower the SEI and charge transfer resistances without the need to alter the SEI phase formation energetics per se.

Figure S2 (Supporting Information) illustrates how external pressure impacts the SEI in terms of the distribution of fluorine on the current collector surface. Analysis was performed on

Table 1. Fitted results of EIS spectra of lithiated and plated Li|Cu cells under various pressure.

Impedance [Ω]	R_{Ohm}	R_{SEI-1}	R_{SEI-2}	$R_{SEI-1} + R_{SEI-2}$	R_{ct}
0.1 MPa (Lithiated)	6.1	3.9	23.5	27.4	13.9
0.1 MPa (Plated)	14.8	3.9	28.5	32.4	11.9
1 MPa (Lithiated)	2.8	6.2	23.8	30	12.4
1 MPa (Plated)	5.8	6.1	29.9	36	12.5
10 MPa (Lithiated)	2.7	5.2	18.2	23.4	10.6
10 MPa (Plated)	2.7	4.9	19.0	23.9	10.6

lithiated (but not plated) half-cells tested at 0.1, 1, and 10 MPa. The figure shows SEM images and the associated EDXS elemental maps of fluorine. A parameter termed "SEI homogeneity" is defined as the ratio of the maximum intensity to the minimum intensity of mapped F, based on image-hue analysis. Within the area mapped, fully homogeneous coverage of the surface by F results in uniform intensity and SEI homogeneity of 1, i.e., 100%. While being able to map the distribution of F over a certain area, this analysis does provide chemical bonding details. Per XPS analysis shown next, within the SEI the relevant phases are LiF, $LiPOF_x$, and $LiPF_x$. When pressure increases from 0.1 to 1 MPa and to 10 MPa, SEI homogeneity increases from 58.7% to 82.3% and to 94.1%.

Figure 2a–c compares top-down optical and SEM images that show the differing Li electrodeposit morphologies that are formed at the three pressures. The electrochemical regiment consisted of a single plating step of 3 mAh cm^{-2} at 1 mA cm^{-2} onto an empty Cu collector. It may be observed that the electrodeposit microstructure and surface topography are strongly affected by static pressure. Per 2(a), it may be observed that at 0.1 MPa the electrodeposit microstructure consists of an interconnected network of metal, SEI, and micron-scale pores. The electrodeposit covers less than half of the collector and is blackish in color. Per 2(b) at 1 MPa the electrodeposit is microscopically less porous, giving it a visible metallic luster. Macroscopically the electrodeposit covers more of the collector surface than did the 0.1 MPa specimen. Per 2(c) at 10 MPa the electrodeposit is most favorable in terms of film continuity and morphology. With increasing pressure the electrodeposit covers more of the collector surface, has less pores in its bulk, and displays a lower surface roughness. However, it may be observed that an external pressure of 10 MPa is sufficient to physically tear the PP separator. As shown in 2(c), about half of the electrodeposit remained on the Cu foil surface while the other half adhered to the torn PP separator. Figure S3a (Supporting Information) shows SEM images of an unused PP separator shown as a baseline for comparison. Figure S3b,c (Supporting Information) provides SEM images of PP separator extracted from half-cells cells tested at 1 MPa. Figure S3d–f (Supporting Information) shows SEM images of PP separator extracted from 10 MPa cells, displaying the adherent solid residue.

An external pressure of 10 MPa is not practically feasible, both due to the engineering complexity required for achieving it in conventional pouch cells, and because it results in the tearing of the polyolefin separator. In fact, high-pressure induced separator tearing has been identified to cause cell internal short circuits (ISCs).[28] Figure S4 (Supporting Information) shows a voltage profile of a baseline Cu half-cell, cycled at 10 MPa. The abrupt voltage drop is indicative of a cell short, agreeing with the observed PP separator tearing. To further probe this effect, a series of experiments were carried to determine the external pressure for causing ISC. As shown in Figure S5 (Supporting Information), at 10 MPa an abrupt voltage drop is observed in baseline Cu half-cells for plating less than 20 min at 1 mA cm^{-2}. Lowing the current density to 0.2 mA cm^{-2}, ISC occurs after 40 min of plating. While plating/stripping at 0.2 mA cm^{-2} and 1 MPa is stable, when the pressure is increased to 10 MPa a short almost immediately follows. This experiment is shown in Figure S6 (Supporting Information). The results point to the critical static pressure for mechanical-stress driven ISC being on the order of 10 MPa, expectedly independent of the applied current.

Figure 2d–l presents the C 1s and F 1s XPS spectra of the plated Li surfaces at the three pressures. With pressure increasing from 0.1 to 10 MPa there is a significant decrease in the C—O peak (286 eV in C 1s) and C=O peak (RO—CO_2Li, 288.4 eV) intensity. However, with increasing pressure, there is an increase in the F 1s intensity, with the $LiPOF_x$/$LiPF_x$ peaks being prominent at 10 MPa. The C—O/C=O species originate from the reduction of the carbonate solvent. These F-containing species are formed by the reduction of FEC and $PF6^-$. It is known that $LiPOF_x$/$LiPF_x^-$ is a product of $PF6^-$ decomposition, and will further decompose to form LiF. As will be demonstrated by sputter-down XPS analysis, the $LiPOF_x$/$LiPF_x^-$ products primarily exist on the topmost surface of the SEI. The additive FEC decomposes to yield not only LiF but also Li_2CO_3 + F-containing organic species (C—F and C—F_2), while solvents in the electrolyte, e.g. EC, DEC, decompose to give RO—CO_2—Li, and C—O species.[29] The results indicate that at higher static pressure there is a propensity for relatively more PF_6^- decomposition, yielding a more inorganic-rich SEI. Increased SEI homogeneity and a more inorganic-rich SEI are beneficial for electrochemical stability, especially if the result is a more uniformly distributed LiF phase.[30]

With increasing pressure, the decomposition of carbonate solvents (EC/DMC/EMC/FEC) on the Li surface may be suppressed, allowing for FEC and anion reduction products to preferentially accumulate. This trend is validated by XPS depth profiling experiments shown in Figure 2d–l. For Li deposits formed at 10 MPa, after removing the top layer by Ar^+ etch, intense LiF and Li_2CO_3 peaks are present. Conversely, the Li deposited at 0.1 MPa exhibits intense RO—CO_2Li, C—O signals even after the removal of the top layer. For 10 MPa specimens, underlying Li metal is detected after etching, as demonstrated by the discernable Li^0 peak. For the 0.1 MPa specimen, after the same etching regiment the Li^0 peak is absent, indicating that the SEI is thicker. Interestingly, these results diverge from what was reported in a recent study where the SEI components were found to be nearly identical at different external pressures.[20] This can understood in terms of the electrolytes that were employed: The earlier study utilized a high-salt-concentration ether-based electrolyte (4.6 m LiFSI and 2.3 m LiTFSI in DME) that is known to yield an inherently more stable SEI than with carbonate electrolytes. With 1 M $LiPF_6$ in EC:DEC:EMC, the SEI structure should be more affected by cycling conditions such as plated/stripped capacity, current density, net number of cycles, temperature, and external pressure.

To further probe the electrodeposition behavior of Li and its relation to external pressure and the SEI, we employed a lithiophilic secondary current collector and repeated the experiments at 1 MPa. The secondary current collector was based on a graphene layer with minimum defects, termed pristine graphene (pG). Lithiated multilayer graphene is known to be lithiophilic,[31] while minimizing its defect content impedes further carbonate decomposition and promotes SEI stability. Figure S7a–c (Supporting Information) shows coupled atomic force microscopy (AFM)-Raman analysis of pG. Figure S7a (Supporting Information) shows the AFM image overlaid with height profiles associated with the line scans. The apparent height of monolayer graphene as probed by AFM is known to be in the range of 0.8–1.5 nm, depending on the substrate, tip and measurement

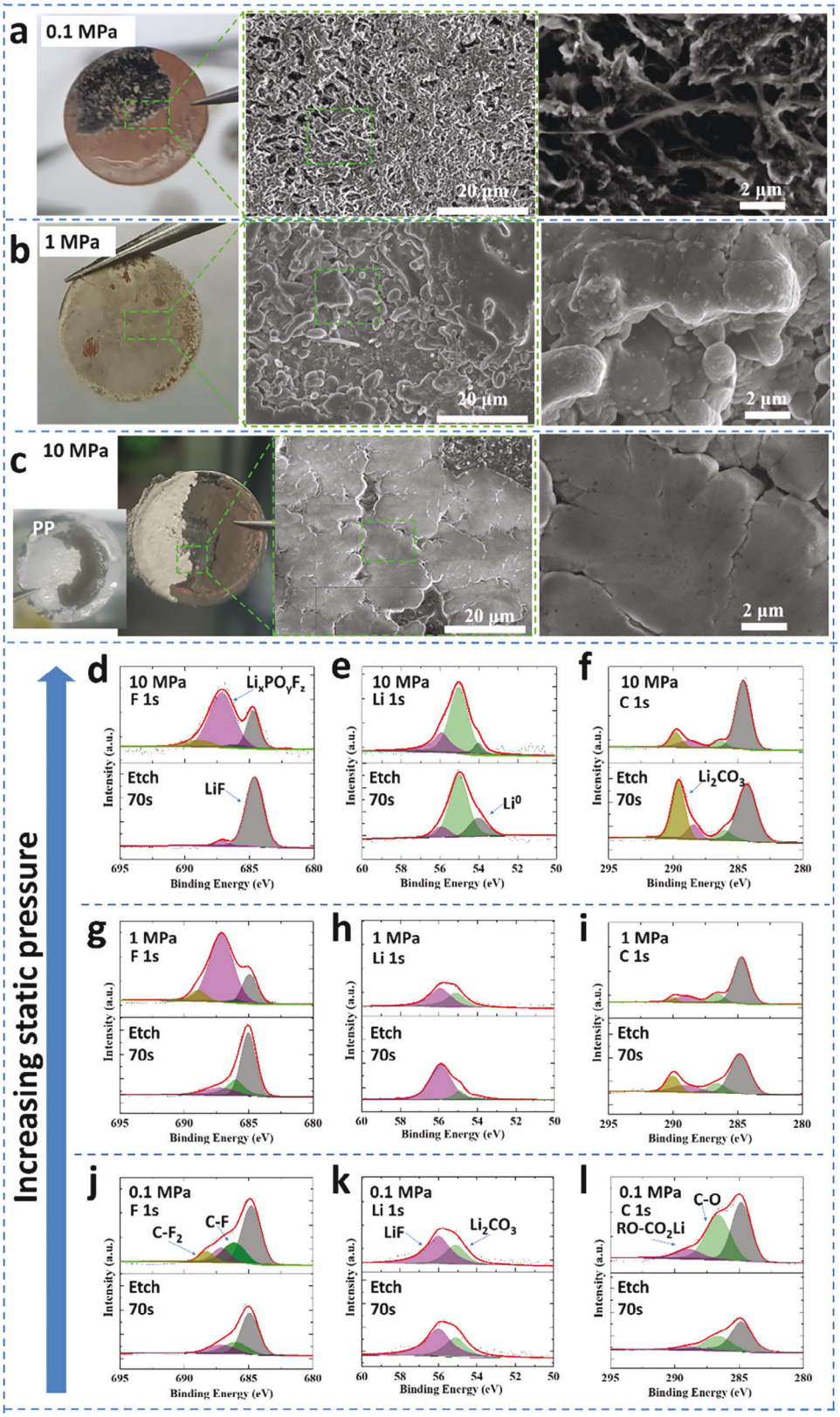

Figure 2. Analysis of lithium plated onto a Cu collector in a half-cell, capacity of 3 mAh cm^{-2} at 1 mA cm^{-2}. a–c) Low magnification optical light microscope images and high magnification SEM images of the Li metal surface, at 10, 1, and 0.1 MPa, respectively. d–f) XPS F 1s, Li 1s and C 1s spectra comparing the SEI structure at 10 MPa. g–i) Same analysis but at 1 MPa. j–l) 0.1 MPa. In the three cases, 70 s of Ga^+ ion depth profiling was employed to remove the topmost SEI, exposing the inner SEI and the metallic Li^0 underneath.

parameters, etc.[32] The pG sheets analyzed were measured to be 5–6 nm thick, indicating that they consist of 3–5 graphene monolayers. Figure S7b,c (Supporting Information) displays the Raman spectra from three different spots, all demonstrating ordered graphene structures with minimal defects. The integrated strong D band intensity to G band intensity ratios were 0.09, 0.07, and 0.11. Figure S8a–d (Supporting Information) presents the cross-sectional view and top-down view SEM images of pG coated onto a Cu foil. The total thickness of the coating was 5–6 μm, with a mass loading in the range of 0.5 mg cm^{-2}. This is the architecture employed as a seeding layer for Li plating and was termed pG@Cu. An external pressure of 1 MPa was employed for these experiments.

The pG@Cu half-cell underwent a single lithiation-delithiation step at 50 μA cm^{-2} through a voltage range of 0.01–3 V versus Li/Li^+, as shown in **Figure 3**a. Per Figure S9a (Supporting Information) the first lithiation and de-lithiation capacities were 470 and 196 μAh cm^{-2}. The irreversible capacity of 274 μAh cm^{-2} is due to SEI formation and some irreversible trapping of the Li in the limited structural defects of the carbon.[33] Figure S9b (Supporting Information) shows the EIS Nyquist plots of the pG@Cu electrode in the lithiated state to 0.01 V versus Li/Li^+, and in the plated state to 3 mAh cm^{-2}. Table S1 (Supporting Information) provides the fitted parameters of the Nyquist plots. One semi-circle is observed that is ascribed to a combination of R_{SEI} and R_{ct}. Transitioning from a lithiated state to plated state the Ohmic resistance (R_{Ohm}) remains almost unchanged, 6.69 to 6.9 Ω. Upon plating there is also a minimal increase in the R_{SEI} + R_{ct}, going from 53.9 to 55.2 Ω. Figure 3b shows a cross-section SEM image of pG@Cu after it was lithiated–delithiated. The cross-section was obtained by Ar^+ ion milling, employing a vacuum transfer holder. It may be observed that the pG layer remains ≈ 5 μm thick, despite being now covered by the SEI. The layer has partially separated from the Cu support, which may have occurred during sample preparation. As expected, the Cu foil surface morphology was not altered from its as-received state. While being macroscopically flat, the foil is rough on the micron scale, as is demonstrated in the figure. Such a surface topography is representative of the Cu current collector foil morphology in general and is consistent with numerous reports.[34]

Figures 3c,d present the top-down SEM images and corresponding EDXS maps of C, O, and F for pG@Cu and baseline Cu surfaces after one lithiation–delithiation. The SEI layer formed on the surface of pG@Cu has a relatively uniform morphology, the magnification marker being 25 microns. The EDXS maps show a uniform C, O, and F distribution. As shown in Figure 3d, the SEI formed on top of baseline Cu is highly nonuniform, being present in clumps that display varied intensity in the EDXS maps. Figure 3e displays XPS sputtering depth profiles of pG@Cu after the lithiation–delithiation. Per the analysis of F 1s, the F-containing SEI components are C—F (686.1 eV), $Li_zPO_yF_x$ (686.9 eV), and LiF (685.0 eV). With increased sputtering time (depth), the LiF-related signal intensity became the most dominant. The C—O (532.0 eV in O 1s and 286.1 eV in C 1s) and C═O peaks (530.5 eV in O 1s and 288.4 eV in C 1s) are detected at the top surface of the SEI. In general, carbonate solvents, including EC, DEC, EMC, and FEC, have relatively high LUMO (lowest unoccupied molecular orbital). Hence, the Li^+-solvent complexes have a strong tendency to be reduced through ring-opening and decarboxylation reaction routes. This results in SEI components Li_2O/Li_2CO_3, ROLi (lithium alkoxide), $ROCO_2Li$ (lithium oxidate alkyl carbonates), and C—F compounds. In contrast, the anion PF_6^- decomposes to give Li_xPF_y, LiF species.[4d,35] In general, Li_2O/Li_2CO_3/F—C species originate from carbonate solvent (EC/DEC/EMC/FEC) reduction while LiF inorganics are derived from anion (PF_6^-) reduction. This indicates that the highly ordered structure of pG leads to suppressed decomposition of solvents, allowing more PF_6^- anion decomposition products (Li_xPF_y and LiF) to precipitate on the surface. These anion-derived species are well-known to promote electrochemical stability in Li metal anodes, with LiF being a key component of a stable SEI structure.[30,36]

Figure 4a,b displays cross-section SEM images of pG@Cu after a single plating step of 3 mAh cm^{-2} capacity at 1 mA cm^{-2} current density. On pG@Cu the Li electrodeposit is relatively dense, at approximately 19 microns thickness versus 15 microns based on theoretical density. While there is substantial porosity in the underlying pG, the polycrystalline Li metal plated on top of it is nearly fully dense. There is some surface roughness in the film that is likely associated with crystallite growth velocity differences (e.g., [001] Li growing faster than [110] Li, or vice versa). Figure 4d–e highlight Li plated onto the baseline Cu foil at identical conditions. The resultant electrodeposit layer is ≈52 micrometers thick and is composed of filament-like Li metal interspersed with pores and with SEI.

Cryo-stage transmission electron microscopy (cryo-TEM) was performed on the pG@Cu and baseline Cu metal electrodeposits. Argon ion milling coupled with a vacuum sample holder was employed for electrode sectioning, sample preparation details being provided in the Supplementary information. Figure S10 (Supporting Information) compares the SEM and low-magnification TEM images of Li deposits that were transferred from Cu foil onto Cu grids. Figure 4c,f compares the microstructure of the SEI layers formed with the two supports. The associated FFTs highlight the crystalline component of SEI, being nano-sized Li_2CO_3 embedded on an amorphous matrix. As may be observed, the SEI on pG@Cu is sufficiently thin that a (110) oriented FFT from the Li metal is also discernable. It was not possible to find regions in the baseline Cu specimen where both crystalline Li_2CO_3 and Li metal are discernable. The cryo-TEM findings further support the general conclusion that the pG@Cu support promotes more uniform plating of the Li metal and a more uniform SEI. Figure 4g shows the EDXS elemental distribution line scan along the cross-section direction of pG@Cu, while 4(h) displays this analysis for baseline Cu. A comparison of the F, C, and O signals in the two specimens confirms that with the plated Li metal on pG@Cu is dense and does not contain interspersed SEI. With baseline Cu the plated Li is porous and is intermixed with SEI throughout the entire thickness.

Density functional theory (DFT) calculations were performed to further understand the plating process and the role of pG versus baseline Cu as support. As shown in **Figure 5**e–g, the relevant orientations of Cu are <100>, <110>, and <111>, being standard fiber textures observed in fcc metals. Figure 5h shows the <0001> orientation of graphene, which is what is relevant for the support employed. Figure 5 dalso displays the top-down view of ethylene carbonate (EC) solvated Li^+ as the adsorbent ($Li^+(EC)_4$),

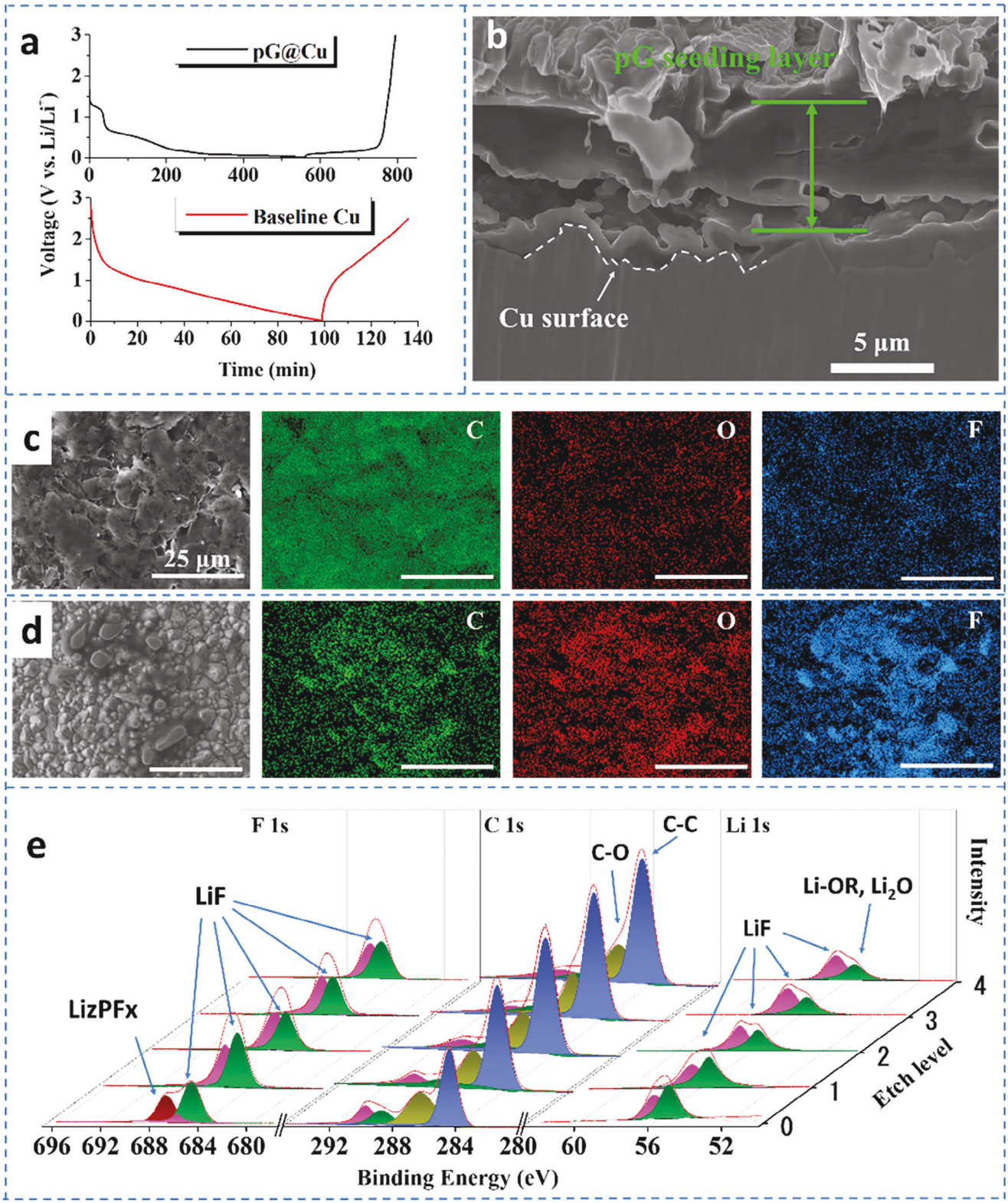

Figure 3. a) Voltage profiles of pG@Cu and baseline Cu half-cells, single lithiation-delithiation 0.01–3 V at 50 μA cm^{-2}. b) Side-view cross-section SEM images of pG@Cu electrode. c) SEM and EDXS elemental maps of the pG@Cu surface. d) the same analysis for baseline Cu. Scale bars represent 25 μm. e) XPS depth profiling of F1s, O1s, C1s, and Li 1s spectra on the pG@Cu after the lithiation-de-lithiation step.

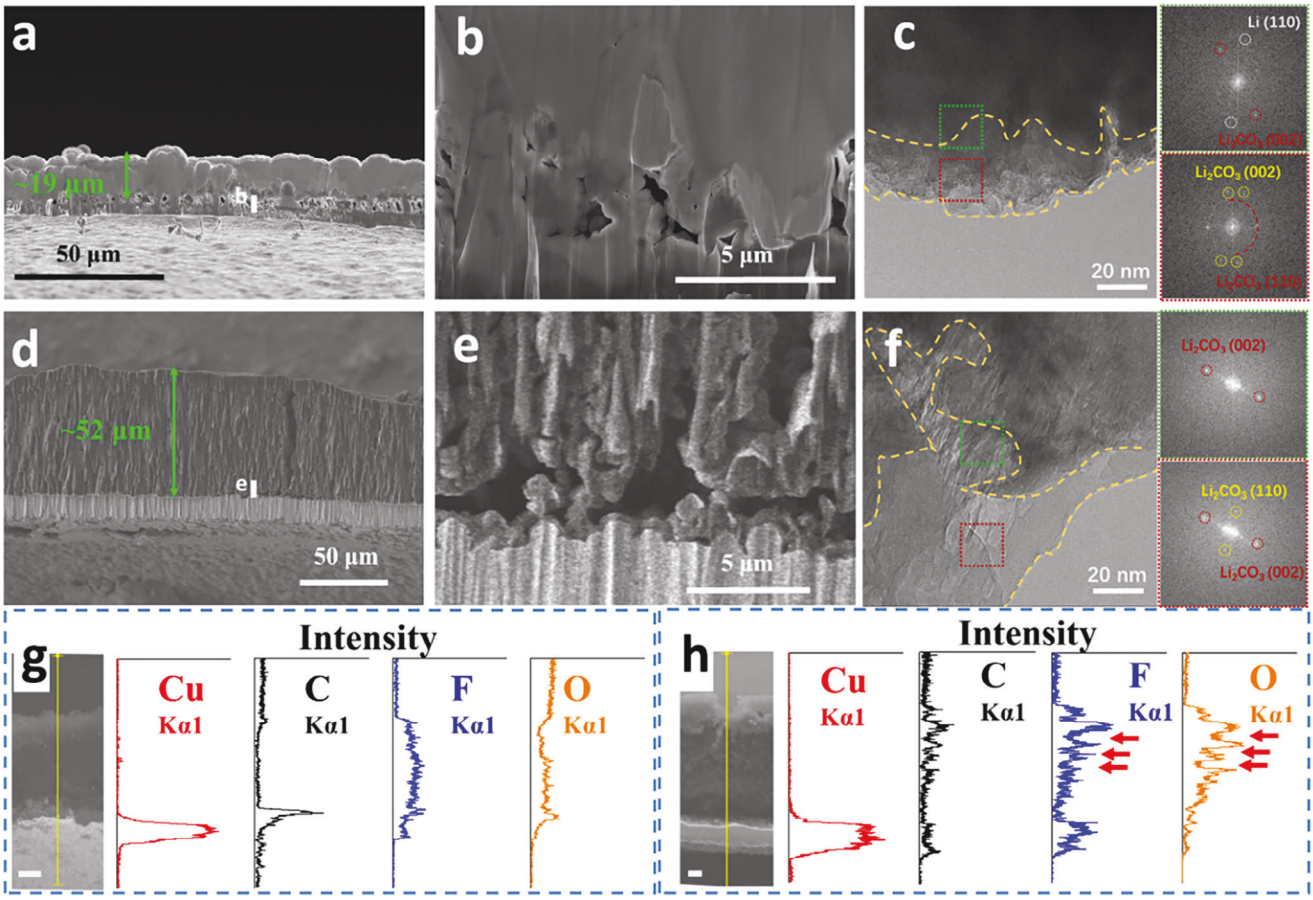

Figure 4. a,b) Cross-section SEM images of Li plated onto pG@Cu half-cell. c) Cryo-TEM analysis of Li electrodeposits on pG@Cu with Fast Fourier Transform (FFT) patterns of the bulk metallic Li region (green) and the SEI regions (red) shown as the insets, Li-deposits were prepared in a half-cell configuration at 3 and 1 mA cm^{-2}. d–h) Same analysis performed on the Li plated onto baseline Cu. g) EDXS elemental distribution line scan along the cross-section direction of pG@Cu. h) Same analysis for baseline Cu. Scale bar 5 µm.

which is a representative Li solvation structure in 1 M $LiPF_6$ electrolyte. Figure 5e–h displays the binding of anion PF_6^- with the three Cu facets and with graphene. As shown in **Table 2**, with adsorbent $Li(EC)_4$, all three Cu facets display significantly more negative adsorption energy than the graphene, with (100) being the most favored. From the calculated results it may be observed that the trend is the opposite with PF_6^-. The least positive adsorption energy is on (0002) pG, indicating that it is the preferred surface for its adsorption and subsequent decomposition into F-containing reduction products discussed earlier. The thermodynamic preference of (0002) pG for PF_6^- adsorption over the Cu surfaces explains its preference for F-containing SEI phases.

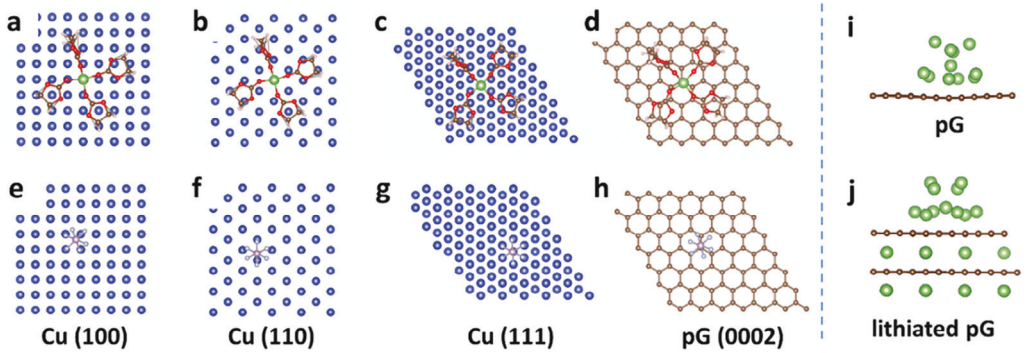

Figure 5. a–d) Density functional theory (DFT) analysis. Top-down view of the representative structures of solvated-Li^+ ($Li^+(EC)_4$) on (100)Cu, (110)Cu, (111)Cu, and (0001)pG surfaces. e–h) Top-down view of adsorbed anion (PF_6^-) on these surfaces. i–j) Adsorbed nuclei of Li-cluster on the surface of pG and lithiated pG, respectively. Color scheme: Li (green), O (red), C (brown), F (silver) and P (light purple).

Table 2. Adsorption energies of representative species in carbonate electrolyte on Cu and pG.

	Cu (100)	Cu (110)	Cu (111)	pG (0002)
$Li^+(EC)_4$	−4.98 eV	−4.76 eV	−5.27 eV	−3.81 eV
PF_6^-	2.12 eV	2.70 eV	2.62 eV	1.51 eV

The result that the (100), (110), and (111) Cu facets display significantly different solvent and salt adsorption energies helps to explain the heterogeneity of the SEI. The rolled Cu foil is expected to have a range of orientations, each with its own propensity for molecule adsorption and decomposition. The graphene layers, conversely, are oriented with the basal planes exposed, resulting in uniform adsorption energetics. This is a key advantage of pG; that the adsorption energy for both solvent and salt molecules remains constant with position, unlike with polycrystalline Cu where it varies with the orientation of the individual grains. The grain size of Cu foils is in the order of ten microns or less, qualitatively agreeing with the scale of the SEI topography shown in Figure S2 (Supporting Information).

Finally, the role of non-lithiated versus lithiated pG was examined. A lithium cluster consisting of 11 Li atoms was employed as the initial nuclei. Figure 5i–j demonstrates more favorable Li nuclei adsorption on the (0001) surface of lithiated pG (−3.57 eV) versus on a non-lithiated (i.e., pristine) surface (−2.24 eV). This indicates that intercalation of Li into graphene should promote enhanced adsorption of Li clusters, leading to enhanced wetting of the Li-layer. After the initial Li layer is deposited, the subsequent metal should grow epitaxially with growth velocities depending on the crystal orientation, while forming additional nuclei as the film thickens. This type of Van der Drift film growth has been detailed in literature both experimentally and through modeling.[37] Therefore, there may be a "memory effect" where the initial wetting behavior of the first few layers of Li on the pG (or the baseline Cu) continuously influences the morphology and texture of the thickening electrodeposit.

To illustrate how the differences in the support structure and the associated SEI influence the electrochemical performance of anode-free lithium metal batteries, experiments were performed on half-cells and on full battery configurations employing NMC811 cathodes. **Figure 6**a–d compares the behavior of pG@Cu|Li and baseline Cu|Li half-cells. It may be observed that with the baseline Cu the overpotential increases with cycle number up to the point of impedance-rise induced failure at ≈20th cycle. While the baseline Cu can only cycle for ≈150 h, the pG@Cu cell displayed stable plating-stripping behavior for over 300 h. In Figure 6b, it may be observed that the CE of baseline Cu rapidly decayed at around cycle 20, while the CE of pG@Cu was stable at ≈ 95.5% throughout the 300 h of cycling. The voltage-capacity profiles of pG@Cu|Li and baseline Cu|Li cells at cycle 1 are shown in Figure 6c. The 1st cycle nucleation overpotential of pG@Cu is 49 mV versus 276 mV for the baseline Cu. According to Figure 6d, during cycling the difference in the nucleation overpotentials still exists, with pG@Cu being 68 mV after 30 cycles, while baseline Cu being 117 mV after 26 cycles.

Figure 6e shows the cycling performances of pG@Cu at current densities of 0.75, 1.5, 3, and 6 mA cm^{-2}. A plating time of 0.5 h was adopted for each cycle, and 20 plate-strip cycles were performed at each current density. For pG@Cu the voltage profiles at each current density are overlapping, indicating stable electrochemical behavior. In contrast, baseline Cu was unstable starting at 0.75 mA cm^{-2}, with the stripped capacity being significantly smaller than what was plated. This is illustrated in Figure 6f. As shown in Figure 6g, at a high current density of 6 mA cm^{-2} the stripping curves become highly fluctuating, indicative of the onset of cell failure. The significant difference in the electrochemical performance of pG@Cu and baseline Cu is further illustrated by comparing the CEs (Figure S11, Supporting Information). The CE of the pG@Cu is consistent throughout cycling, remaining above 90%. The large fluctuations in the CE of baseline Cu, e.g., going from 90% to 30% and back to 80%, is consistent with the observed unstable electrochemical behavior (Figure S12, Supporting Information). This would include a combination of dendrite growth, excessive SEI formation, and possible formation/dissolution of electrically isolated "dead metal". Accurate CE measurements were carried out following the approach outlined in ref.[38] A capacity of 6 mAh cm^{-2} was firstly plated on the working electrode (pG@Cu or baseline Cu) using a current density of 1 mA cm^{-2}. Then 1 mAh cm^{-2} Li was stripped/plated at 1 mA cm^{-2} for 100 cycles. Finally, the electrodeposit was 100% DOD stripped up to a voltage limit of 1 V, also at 1 mA cm^{-2}, at which point the CE was recorded. These results are compared in Figure 6h for pG@Cu and baseline Cu. The pG@Cu displays a CE of 99.8%, while the baseline Cu displays a CE of 91.9%. It should be noted that a CE of 99.8% is very difficult to achieve in carbonate electrolytes. In fact, 99.8% exceeds CEs reported for LMBs with advanced fluoro-ether-based electrolytes.[39]

Figure 7 shows the NCM-based anode-free lithium metal battery (AF-LMB) electrochemical performance adopting pG@Cu and baseline Cu as anode current collectors. The cells were tested at an external pressure of 1 MPa. The mass loading of NCM cathodes was 18 mg cm^{-2} to match with commercial level area capacity of 3.4 mAh cm^{-2} (electrode compaction density = 2.5 g cc^{-1}). Prior to full cell assembly, pG@Cu was pre-lithiated by pressing it against a Li-disc that is wetted by the electrolyte to reduce the cycle 1 CE loss of the AF-LMB. Figure 7a–b shows representative galvanostatic voltage profiles of pG@Cu||NCM and baseline Cu||NCM cells at the initial cycles of C/20-C/20 charge–discharge. The C-rate was calculated based on the cathode capacity, with 1C = 178 and 3.4 mA cm^{-2}. Figure 7c shows the cycling performance of anode-free LMBs at various rates that are marked on the panel. At 0.05, 0.1, 0.2, 0.5, and 1 C the pG@Cu||NCM cells deliver reversible capacities of 3.04, 2.94, 2.74, 2.24, and 1.57 mAh cm^{-2}, with an average working voltage of 3.81, 3.80, 3.78, 3.67, 3.47 V. At 0.2C-charge-0.5C-discharge, the pG@Cu||NCM cell showed an average CE of 99.68% throughout the 30th to 100th cycle, with a capacity retention of 89.5%. In contrast, the baseline Cu||NCM cells displayed rapid capacity decay from the onset of cycling.

The cycling performance of the pG@Cu||NCM cells was tested with even higher mass loading (21.1 mg cm^{-2}) and capacity, using state-of-the-art single-crystal NCM particles. These cells are designated pG@Cu||NCM-S. As compared to what is colloquially termed "meatball" (polycrystalline aggregate) NCM, the

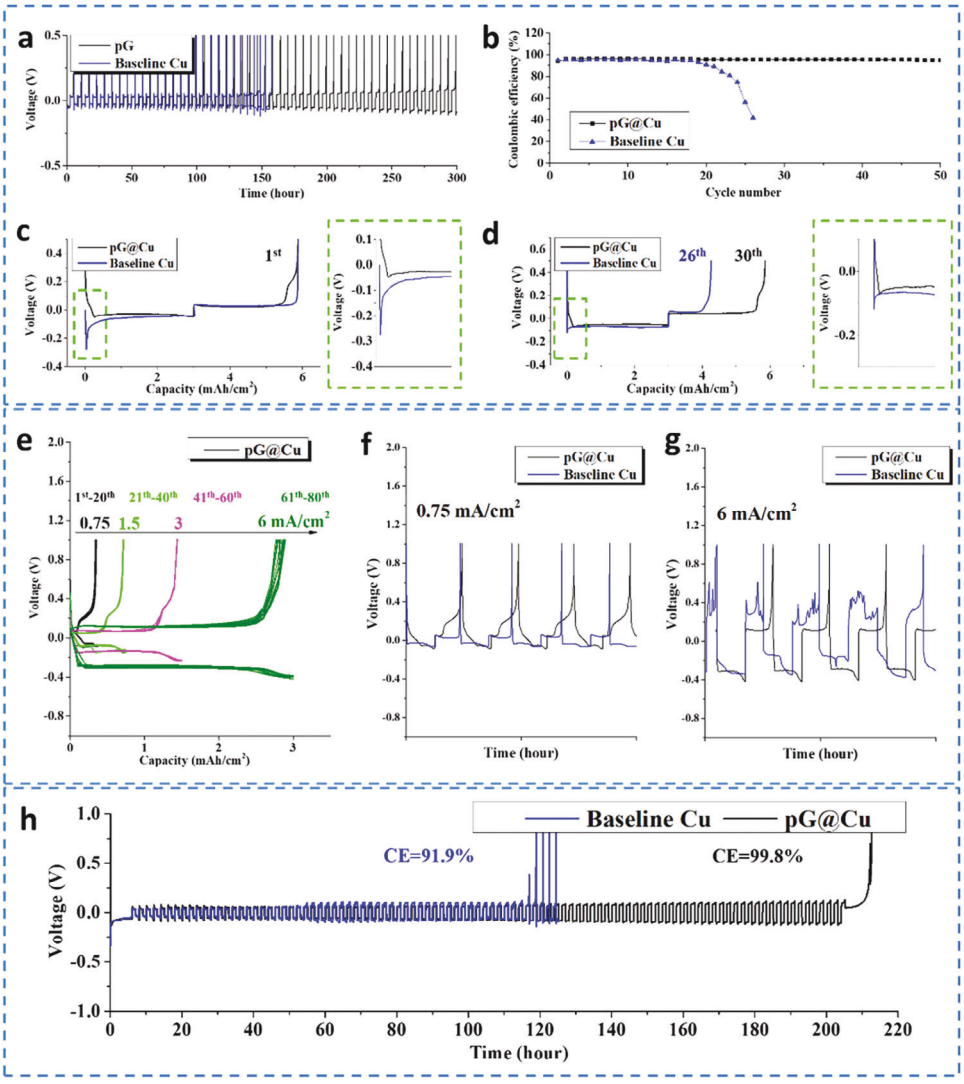

Figure 6. Electrochemical performance comparison of half-cells operating at 1 MPa. a–b) Galvanostatic profiles and the associated CE values of pG@Cu|Li and baseline Cu|Li at 3 mAh cm^{-2}, 1 mA cm^{-2}. c–d) Galvanostatic profiles at 1st and 26th/30th cycle, at 3 mAh cm^{-2}, 1 mA cm^{-2}. e) Voltage-capacity profiles of pG@Cu|Li at various current densities. f),g) Representative profiles at 0.75 mA cm^{-2} and 6 mA cm^{-2}, respectively. h) CE analysis, where 6 mAh cm^{-2} of Li was first deposited as a Li reservoir, then 1 mAh cm^{-2} was stripped/plated at 1 mA cm^{-2} for 100 cycles, followed by 100% DOD stripping.

single crystal NCM particles may be more aggressively calendared. This allowed for a cathode compaction density of 3.4 g cc^{-1}, with 1C being defined as 3.8 mA cm^{-2}. Moreover, for these aggressive tests, the cell electrolyte volume was reduced from 100 to 60 µL. Figure 7d displays the cycling performance of pG@Cu||NCM-S using a constant-current-constant-voltage (CCCV) cycle protocol. This protocol consists of galvanostatic charging at 0.2C followed by potentiostatic charge with 0.05C cut-off and 0.5C discharge. It may be observed that pG@Cu||NCM-S cell displayed good cycling stability with 70.5% capacity retention after 200 cycles (3.87 to 2.73 mAh cm^{-2}). Table S2 (Supporting Information) compares the achieved performance of pG@Cu||NCM-S with state-of-the-art AF-LMBs. It may be observed that the combination of high areal capacity cathode and extended cyclability are overall quite favorable.[14b,15b,18c,40]

3. Conclusion

Anode-free lithium metal batteries (AF-LMBs) employ an "empty" anode current collector to facilitate repeated plating/stripping of lithium metal, with the cathode being the sole source of the shuttling ions. This imposes stringent requirements on the electrodeposition process, making the role of electrolyte interphase (SEI) stability even more critical. Using a unique pressure-controlled liquid electrolyte electrochemical cell, combined with density functional theory simulation, we analyzed the role of external pressure on the geometric heterogeneity and the structure of SEI, correlating it to lithium metal morphology and overall electrochemical stability. Three externally applied pressures were employed; 0.1 MPa which was insufficient for achieving even minimal electrochemical stability on bare Cu,

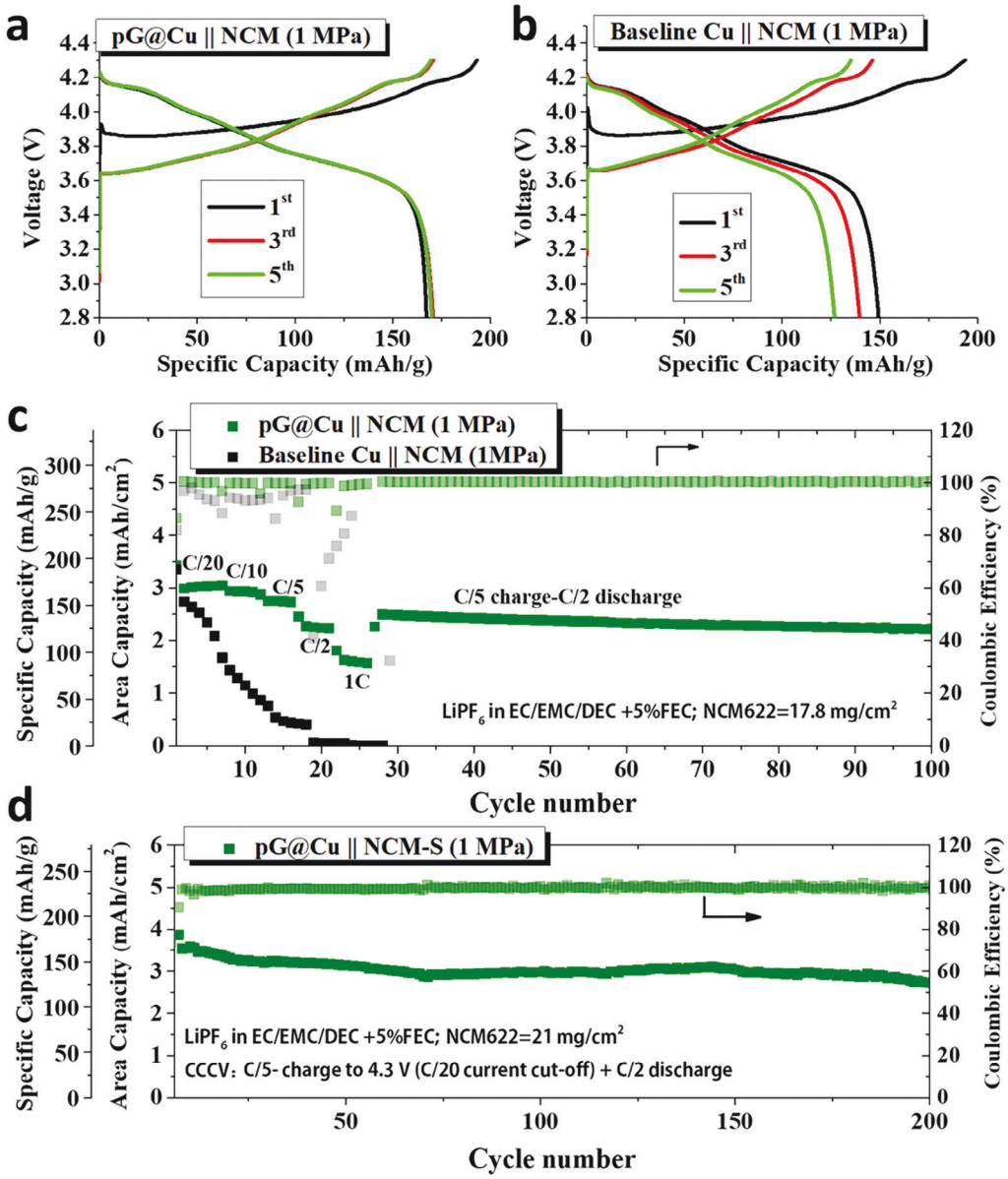

Figure 7. a–b) Galvanostatic voltage profiles of anode-free lithium metal batteries (AF-LMBs) based on pG@Cu||NCM and baseline Cu||NCM cells at the initial cycles of C/20–C/20 charge–discharge. c) Cycling performance of anode-free LMBs at various rates marked on the panel. For a–c) NCM = 17.8 mg cm^{-2}, 1C = 3.4 mA cm^{-2}. d) Cycling performance of AF-MBs based on pG@Cu||NCM-HL, with NCM-S = 21 mg cm^{-2}, 1C = 3.8 mA cm^{-2}.

1 MPa which still led to a non-uniform SEI and dendritic metal electrodeposits at higher current densities, and 10 MPa which despite having the most promising electrochemical signature is practically infeasible for several reasons. In parallel, we considered the role of a lithiated graphene underlayer as a secondary current collector, demonstrating how and why it allowed for stable 1 MPa plating/stripping behavior under otherwise identical conditions. It is demonstrated that with a baseline polycrystalline Cu surface an organic-rich SEI is favored, this being accompanied by filament-like Li metal and extensive porosity. A high external pressure favors inorganic F-rich SEI, accompanied by a uniform and dense Li electrodeposit. It is shown that the lithiated graphene layer favors the same type of an F-rich SEI, but at lower external pressure, promoting uniform metal plating/stripping and stable electrochemistry in half and full cells.

Supporting Information

Supporting Information is available from the Wiley Online Library or from the author.

Acknowledgements

W.L. acknowledges the financial support of the National Key Research and Development Program of China (2022YFE0135900) and Natural Science Foundation of China (51702223). D.M. was supported by the National Science Foundation, Division of Materials Research, Award Number

1938833.The authors thank the Analytical & Testing Center and INELT of Sichuan University for the characterization and simulation toolsets.

Conflict of Interest

The authors declare no conflict of interest.

Data Availability Statement

The data that support the findings of this study are available from the corresponding author upon reasonable request.

Keywords

chemo-mechanics, critical current density (CCD), dendrite, electrochemical-mechanical, pressure, solid electrolyte interphase (SEI)

Received: July 14, 2023
Revised: October 27, 2023
Published online:

[1] a) D. Lin, Y. Liu, Y. Cui, *Nat. Nanotechnol.* **2017**, *12*, 194; b) X.-B. Cheng, R. Zhang, C.-Z. Zhao, Q. Zhang, *Chem. Rev.* **2017**, *117*, 10403; c) F. Han, A. S. Westover, J. Yue, X. Fan, F. Wang, M. Chi, D. N. Leonard, N. J. Dudney, H. Wang, C. Wang, *Nat. Energy* **2019**, *4*, 187; d) Y. Guo, H. Li, T. Zhai, *Adv. Mater.* **2017**, *29*, 1700007.

[2] a) E. Peled, *J. Electrochem. Soc.* **1979**, *126*, 2047; b) D. Aurbach, *J. Power Sources* **2000**, *89*, 206; c) P. Bai, J. Li, F. R. Brushett, M. Z. Bazant, *Energy Environ. Sci.* **2016**, *9*, 3221; d) A. Wang, S. Kadam, H. Li, S. Shi, Y. Qi, *npj Comput. Mater.* **2018**, *4*, 15; e) L. Porz, T. Swamy, B. W. Sheldon, D. Rettenwander, T. Frömling, H. L. Thaman, S. Berendts, R. Uecker, W. C. Carter, Y.-M. Chiang, *Adv. Energy Mater.* **2017**, *7*, 1701003.

[3] a) P. Jiang, Y. Liao, W. Liu, Y. Chen, *J Energy Chem* **2021**, *57*, 131; b) Y.-X. Zhan, P. Shi, X.-X. Ma, C.-B. Jin, Q.-K. Zhang, S.-J. Yang, B.-Q. Li, X.-Q. Zhang, J.-Q. Huang, *Adv. Energy Mater.* **2021**, *12*, 2103291.

[4] a) N.-W. Li, Y.-X. Yin, C.-P. Yang, Y.-G. Guo, *Adv. Mater.* **2016**, *28*, 1853; b) Y. Liu, D. Lin, P. Y. Yuen, K. Liu, J. Xie, R. H. Dauskardt, Y. Cui, *Adv. Mater.* **2017**, *29*, 1605531; c) W. Xu, X. Liao, W. Xu, C. Sun, K. Zhao, Y. Zhao, C. Hu, *Nano Energy* **2021**, *88*, 106237; d) W. Liu, Z. Chen, Z. Zhang, P. Jiang, Y. Chen, E. Paek, Y. Wang, D. Mitlin, *Energy Environ. Sci.* **2021**, *14*, 382.

[5] W. Liu, P. Liu, D. Mitlin, *Chem. Soc. Rev.* **2020**, *49*, 7284.

[6] a) Q.-K. Zhang, X.-Q. Zhang, L.-P. Hou, S.-Y. Sun, Y.-X. Zhan, J.-L. Liang, F.-S. Zhang, X.-N. Feng, B.-Q. Li, J.-Q. Huang, *Adv. Energy Mater.* **2022**, *12*, 2200139; b) X. Cao, P. Gao, X. Ren, L. Zou, M. H. Engelhard, B. E. Matthews, J. Hu, C. Niu, D. Liu, B. W. Arey, C. Wang, J. Xiao, J. Liu, W. Xu, J.-G. Zhang, *Proc. Natl. Acad. Sci. USA* **2021**, *118*, e2020357118; c) J. Zheng, G. Ji, X. Fan, J. Chen, Q. Li, H. Wang, Y. Yang, K. C. Demella, S. R. Raghavan, C. Wang, *Adv. Energy Mater.* **2019**, *9*, 1803774; d) E. Markevich, G. Salitra, F. Chesneau, M. Schmidt, D. Aurbach, *ACS Energy Lett.* **2017**, *2*, 1321; e) X.-Q. Zhang, X.-B. Cheng, X. Chen, C. Yan, Q. Zhang, *Adv. Funct. Mater.* **2017**, *27*, 1605989; f) J. Zhang, M. Zhou, J. Shi, Y. Zhao, X. Wen, C.-C. Su, J. Wu, J. Guo, *Nano Energy* **2021**, *88*, 106298.

[7] a) B. D. Adams, E. V. Carino, J. G. Connell, K. S. Han, R. Cao, J. Chen, J. Zheng, Q. Li, K. T. Mueller, W. A. Henderson, J.-G. Zhang, *Nano Energy* **2017**, *40*, 607; b) L. Suo, W. Xue, M. Gobet, S. G. Greenbaum, C. Wang, Y. Chen, W. Yang, Y. Li, J. Li, *Proc. Natl. Acad. Sci. USA* **2018**, *115*, 1156; c) J. Alvarado, M. A. Schroeder, T. P. Pollard, X. Wang, J. Z. Lee, M. Zhang, T. Wynn, M. Ding, O. Borodin, Y. S. Meng, K. Xu, *Energy Environ. Sci.* **2019**, *12*, 780.

[8] X. Ren, L. Zou, X. Cao, M. H. Engelhard, W. Liu, S. D. Burton, H. Lee, C. Niu, B. E. Matthews, Z. Zhu, C. Wang, B. W. Arey, J. Xiao, J. Liu, J.-G. Zhang, W. Xu, *Joule* **2019**, *3*, 1662.

[9] K. Yan, Z. Lu, H.-W. Lee, F. Xiong, P.-C. Hsu, Y. Li, J. Zhao, S. Chu, Y. Cui, *Nat. Energy* **2016**, *1*, 16010.

[10] K. Wen, L. Liu, S. Chen, S. Zhang, *RSC Adv.* **2018**, *8*, 13034.

[11] C. Yang, Y. Yao, S. He, H. Xie, E. Hitz, L. Hu, *Adv. Mater.* **2017**, *29*, 1702714.

[12] M. Wan, S. Kang, L. Wang, H.-W. Lee, G. W. Zheng, Y. Cui, Y. Sun, *Nat. Commun.* **2020**, *11*, 829.

[13] a) S. Li, M. Jiang, Y. Xie, H. Xu, J. Jia, J. Li, *Adv. Mater.* **2018**, *30*, 1706375; b) S. Kim, G. Park, S. J. Lee, S. Seo, K. Ryu, C. H. Kim, J. W. Choi, *Adv. Mater. n/a*, 2206625.

[14] a) J. Betz, G. Bieker, P. Meister, T. Placke, M. Winter, R. Schmuch, *Adv. Energy Mater.* **2019**, *9*, 1803170; b) S. Nanda, A. Gupta, A. Manthiram, *Adv. Energy Mater.* **2021**, *11*, 2000804.

[15] a) W.-Z. Huang, C.-Z. Zhao, P. Wu, H. Yuan, W.-E. Feng, Z.-Y. Liu, Y. Lu, S. Sun, Z.-H. Fu, J.-K. Hu, S.-J. Yang, J.-Q. Huang, Q. Zhang, *Adv. Energy Mater.* **2022**, *12*, 2201044; b) L. Lin, L. Suo, Y.-S. Hu, H. Li, X. Huang, L. Chen, *Adv. Energy Mater.* **2021**, *11*, 2003709; c) C. Shen, J. Gu, N. Li, Z. Peng, K. Xie, *J. Power Sources* **2021**, *501*, 229969.

[16] a) X. Wang, S. Li, W. Zhang, D. Wang, Z. Shen, J. Zheng, H. L. Zhuang, Y. He, Y. Lu, *Nano Energy* **2021**, *89*, 106353; b) Z. Piao, R. Gao, Y. Liu, G. Zhou, H.-M. Cheng, *Adv. Mater.* **2023**, *35*, 2206009.

[17] P. Liang, H. Sun, C.-L. Huang, G. Zhu, H.-C. Tai, J. Li, F. Wang, Y. Wang, C.-J. Huang, S.-K. Jiang, M.-C. Lin, Y.-Y. Li, B.-J. Hwang, C.-A. Wang, H. Dai, *Adv. Mater.* **2022**, *34*, 2207361.

[18] a) L. Qin, K. Wang, H. Xu, M. Zhou, G. Yu, C. Liu, Z. Sun, J. Chen, *Nano Energy* **2020**, *77*, 105098; b) X. Shen, R. Zhang, P. Shi, X. Chen, Q. Zhang, *Adv. Energy Mater.* **2021**, *11*, 2003416; c) A. J. Louli, M. Genovese, R. Weber, S. G. Hames, E. R. Logan, J. R. Dahn, *J. Electrochem. Soc.* **2019**, *166*, A1291.

[19] a) H. Liu, X. Sun, X.-B. Cheng, C. Guo, F. Yu, W. Bao, T. Wang, J. Li, Q. Zhang, *Adv. Energy Mater.* **2022**, *12*, 2202518; b) X. Zhang, Q. J. Wang, K. L. Harrison, K. Jungjohann, B. L. Boyce, S. A. Roberts, P. M. Attia, S. J. Harris, *J. Electrochem. Soc.* **2019**, *166*, A3639.

[20] C. Fang, B. Lu, G. Pawar, M. Zhang, D. Cheng, S. Chen, M. Ceja, J.-M. Doux, H. Musrock, M. Cai, B. Liaw, Y. S. Meng, *Nat. Energy* **2021**, *6*, 987.

[21] a) S. Yan, X. Xiao, X. Huang, X. Li, Y. Qi, *Polymer* **2014**, *55*, 6282; b) H. Cui, Y. Song, L. Sheng, L. Wang, H. Xu, G. Tian, X. He, *J. Taiwan Inst. Chem. Eng.* **2021**, *119*, 269; c) J. Cannarella, X. Liu, C. Z. Leng, P. D. Sinko, G. Y. Gor, C. B. Arnold, *J. Electrochem. Soc.* **2014**, *161*, F3117.

[22] Y. Wang, Y. Liu, M. Nguyen, J. Cho, N. Katyal, B. S. Vishnugopi, H. Hao, R. Fang, N. Wu, P. Liu, P. P. Mukherjee, J. Nanda, G. Henkelman, J. Watt, D. Mitlin, *Adv. Mater.* **2023**, *35*, 2206762.

[23] a) P. Biswal, S. Stalin, A. Kludze, S. Choudhury, L. A. Archer, *Nano Lett.* **2019**, *19*, 8191; b) A. Pei, G. Zheng, F. Shi, Y. Li, Y. Cui, *Nano Lett.* **2017**, *17*, 1132.

[24] E. Kazyak, M. J. Wang, K. Lee, S. Yadavalli, A. J. Sanchez, M. D. Thouless, J. Sakamoto, N. P. Dasgupta, *Matter* **2022**, *5*, 3912.

[25] C. Yuan, W. Lu, J. Xu, *Adv. Energy Mater.* **2021**, *11*, 2101807.

[26] E. Peled, D. Golodnitsky, G. Ardel, *J. Electrochem. Soc.* **1997**, *144*, L208.

[27] S. Menkin, C. A. O'keefe, A. B. Gunnarsdóttir, S. Dey, F. M. Pesci, Z. Shen, A. Aguadero, C. P. Grey, *J Phys Chem* **2021**, *125*, 16719.

[28] C. Yuan, L. Wang, S. Yin, J. Xu, *J. Power Sources* **2020**, *467*, 228360.

[29] a) E. Markevich, G. Salitra, D. Aurbach, *ACS Energy Lett.* **2017**, *2*, 1337; b) H. Li, Z. Chen, Z. Kang, W. Liu, Y. Chen, *Energy Storage Mater.*

2023, *56*, 40; c) C. Xu, F. Lindgren, B. Philippe, M. Gorgoi, F. Björefors, K. Edström, T. Gustafsson, *Chem. Mater.* **2015**, *27*, 2591.
[30] W. Liu, P. Liu, D. Mitlin, *Adv. Energy Mater.* **2020**, *10*, 2002297.
[31] a) J. Duan, Y. Zheng, W. Luo, W. Wu, T. Wang, Y. Xie, S. Li, J. Li, Y. Huang, *Natl Sci Rev* **2020**, *7*, 1208; b) P. Shi, T. Li, R. Zhang, X. Shen, X.-B. Cheng, R. Xu, J.-Q. Huang, X.-R. Chen, H. Liu, Q. Zhang, *Adv. Mater. 0*, 1807131.
[32] C. Backes, T. M. Higgins, A. Kelly, C. Boland, A. Harvey, D. Hanlon, J. N. Coleman, *Chem. Mater.* **2017**, *29*, 243.
[33] a) E. Memarzadeh Lotfabad, P. Kalisvaart, A. Kohandehghan, D. Karpuzov, D. Mitlin, *J. Mater. Chem. A* **2014**, *2*, 19685; b) W. Liu, P. Li, W. Wang, D. Zhu, Y. Chen, S. Pen, E. Paek, D. Mitlin, *ACS Nano* **2018**, *12*, 12255.
[34] a) Y.-J. Kim, S. H. Kwon, H. Noh, S. Yuk, H. Lee, H. S. Jin, J. Lee, J.-G. Zhang, S. G. Lee, H. Guim, H.-T. Kim, *Energy Storage Mater.* **2019**, *19*, 154; b) C.-C. Lin, Z. Chen, H. Euchner, T. Eisenmann, K. Geng, T. Diemant, S. Fang, C.-H. Yen, S. Passerini, C.-C. Hu, D. Bresser, *ACS Appl. Energy Mater.* **2023**, *6*, 2140; c) Y. Liu, D. Gao, H. Xiang, X. Feng, Y. Yu, *Energy Fuels* **2021**, *35*, 12921.
[35] D. Aurbach, B. Markovsky, A. Shechter, Y. Ein-Eli, H. Cohen, *J. Electrochem. Soc.* **1996**, *143*, 3809.
[36] O. B. Chae, B. L. Lucht, *Adv. Energy Mater.* **2023**, 2203791.
[37] a) C. Ophus, E. J. Luber, D. Mitlin, *Phys Rev E* **2010**, *81*, 011601; b) A. Vanderdrift, *Philips Res. Rep.* **1967**, *22*, 267.
[38] B. D. Adams, J. Zheng, X. Ren, W. Xu, J.-G. Zhang, *Adv. Energy Mater.* **2018**, *8*, 1702097.
[39] a) W. Xue, R. Gao, Z. Shi, X. Xiao, W. Zhang, Y. Zhang, Y. G. Zhu, I. Waluyo, Y. Li, M. R. Hill, Z. Zhu, S. Li, O. Kuznetsov, Y. Zhang, W.-K. Lee, A. Hunt, A. Harutyunyan, Y. Shao-Horn, J. A. Johnson, J. Li, *Energy Environ. Sci.* **2021**, *14*, 6030; b) L. Dong, Y. Liu, K. Wen, D. Chen, D. Rao, J. Liu, B. Yuan, Y. Dong, Z. Wu, Y. Liang, M. Yang, J. Ma, C. Yang, C. Xia, B. Xia, J. Han, G. Wang, Z. Guo, W. He, *Adv. Sci.* **2022**, *9*, 2104699; c) Z. Li, Y. Chen, X. Yun, P. Gao, C. Zheng, P. Xiao, *Adv. Funct. Mater. n/a*, 2300502; d) Y. Ye, Y. Zhao, T. Zhao, S. Xu, Z. Xu, J. Qian, L. Wang, Y. Xing, L. Wei, Y. Li, J. Wang, L. Li, F. Wu, R. Chen, *Adv. Mater.* **2021**, *33*, 2105029.
[40] a) L. Su, H. Charalambous, Z. Cui, A. Manthiram, *Energy Environ. Sci.* **2022**, *15*, 843; b) M. Mao, X. Ji, Q. Wang, Z. Lin, M. Li, T. Liu, C. Wang, Y.-S. Hu, H. Li, X. Huang, L. Chen, L. Suo, *Nat. Commun.* **2023**, *14*, 1082; c) Z. T. Wondimkun, W. A. Tegegne, J. Shi-Kai, C.-J. Huang, N. A. Sahalie, M. A. Weret, J.-Y. Hsu, P.-L. Hsieh, Y.-S. Huang, S.-H. Wu, W.-N. Su, B. J. Hwang, *Energy Storage Mater.* **2021**, *35*, 334.